Size Engineering and Crystallinity Control Enable High-Capacity Aqueous Potassium-Ion Storage of Prussian White Analogues

Chang Li,[a] Xusheng Wang,[b] Wenjun Deng,[a] Chunyi Liu,[a] Jitao Chen,[c] Rui Li,*[a] and Mianqi Xue*[b]

Aqueous potassium-ion batteries have demonstrated huge potential in the field of energy storage, owing to their low cost, environmental friendliness, and high safety, yet with poor cycling stability and rate capability. Here, potassium Prussian white analogues (K-PW) with different gradients in crystallinity and size have been synthesized by controlling the acidity of hydrothermal environment. The as-synthesized $K_{1.93}Fe[Fe(CN)_6]_{0.97} \cdot 1.82H_2O$ nanoparticles deliver considerable reversible capacities of 142 mAh g^{-1} at 75 mA g^{-1}, even 40 mAh g^{-1} at 9000 mA g^{-1}, and high capacity retention of 88% after 300 cycles at 1500 mA g^{-1} in a KNO$_3$ aqueous electrolyte. High crystallinity and short ion-diffusion length determine the fast ion-intercalation kinetics and, thus, enable the superior rate capability. These results reveal the feasibility of using K-PW for practical applications in aqueous potassium-ion batteries.

1. Introduction

Lithium-ion battery (LIB) technologies show strong domination in the highly competitive energy-storage market, while building other new chemistries to realize high power density, long cycling life, and low-cost energy storage is the next critical step.[1] At present, out of many possible electrochemical devices available (such as supercapacitor,[2] lithium-air,[3] lithium-sulfur,[4] and multivalent-ion battery technologies including Mg^{2+}, Zn^{2+}, Ca^{2+}, and Al^{3+}),[5] sodium- and potassium-ion battery (SIB and KIB, respectively)[6] systems are regarded as two of the most promising options owing to the advantages of rich natural abundance of sodium and potassium. Yet while SIB has been widely studied in the last few years, KIB is still in its infancy.

Meanwhile, aqueous systems have attracted considerable attention in the field of electrochemical energy storage, due mainly to their strengths of low cost, environmental friendliness, superior ion-transport property, and high safety.[6d,7] Thus aqueous KIB with high standard redox potential and smallest hydrated ionic radius of potassium is highlighted among the three battery-used alkali metals.[8] Nevertheless, the development of aqueous and even non-aqueous KIBs are hindered by high-performance electrode materials, which should be long-

life cycled against the large volume expansion-contraction that occurs during the charge-discharge processes. The breakthrough study arrived with the use of Prussian white analogues as electrode materials with large interlayer spacing (larger than most layered electrode materials).[7b,9] Reversible K$^+$ insertion/extraction can be realized with no obvious structural damage, thus leading to the high capacity and long-term cycling stability of aqueous KIB. For example, Cui et al. reported the successful synthesis of Prussian blue $K_{0.71}Cu[Fe(CN)_6]_{0.72}$ (CuHCF) material as KIB cathode yet only with a specific capacity of 59 mAh g^{-1} at 0.83 C in a KNO$_3$ aqueous electrolyte.[9a] Su and co-workers prepared the $K_2FeFe(CN)_6$ nanocubes with improved capacity delivery of 120 mAh g^{-1} in the aqueous electrolyte system.[7b] Although excellent progresses in battery performances have been achieved, the combination of high capacity delivery, long cycling life, and high rate capability has not yet been implemented in the previous works, and the difficulty to realize this goal is the dissolution issue of active material in the aqueous electrolyte.[10]

Generally, high crystallinity favors the structural stability of electrode material, which has been demonstrated in the perovskite materials,[11] conducting polymers,[12] organic superconductors,[13] and other unstable systems. Therefore, the preparation of high-crystallinity materials can address the dissolution issue to improve the structural and then cycling stability. Combined with the nano-size engineering, which can provide excellent buffer to structural damage and short ion-diffusion/electron-transfer lengths,[9b] long cycling life and high rate capability can be achieved in aqueous KIBs. In this study, potassium Prussian white analogues (K-PW) with different crystallinity are synthesized via size-regulation hydrothermal method by controlling the acidic environment. As-fabricated $K_{1.93}Fe[Fe(CN)_6]_{0.97} \cdot 1.82H_2O$ nanoparticles demonstrate reversible capacities of 142 mAh g^{-1} at 75 mA g^{-1}, 130 mAh g^{-1} at 300 mA g^{-1}, and even 40 mAh g^{-1} at 9000 mA g^{-1}, and realize

[a] C. Li, W. Deng, C. Liu, Prof. R. Li
School of Advanced Materials, Peking University Shenzhen Graduate School, Shenzhen, 518055, People's Republic of China
E-mail: lirui@pkusz.edu.cn
[b] Dr. X. Wang, Prof. M. Xue
Technical Institute of Physics and Chemistry, Chinese Academy of Sciences, Beijing, 100190, People's Republic of China
E-mail: xuemq@mail.ipc.ac.cn
[c] Prof. J. Chen
Beijing National Laboratory for Molecular Sciences, College of Chemistry and Molecular Engineering, Peking University, Beijing, 100871, People's Republic of China

admirable capacity retention of 88 % after 300 cycles at 1500 mA g^{-1} in a KNO$_3$ aqueous electrolyte, which are superior to those of other reported K-PW materials. The combination of high crystallinity and nano-size engineering offers a new insight into the design and synthesis of high-performance electrode materials for aqueous KIBs and other battery systems.

2. Results and Discussion

In this work, different concentrations of hydrochloric acid aqueous solution (0, 0.2, 0.5, 1.0, 1.5, and 2.0 mol L^{-1}) were used to produce gradient acidic environments. Based on the concentrations of hydrochloric acid, these six prepared samples were separately labelled as KFe(0), KFe(0.2), KFe(0.5), KFe(1.0), KFe(1.5), and KFe(2.0). To affirm the structures of these samples, their X-ray diffraction (XRD) patterns are collected and exhibited in Figure 1a. The KFe(0) sample displays a monoclinic structure
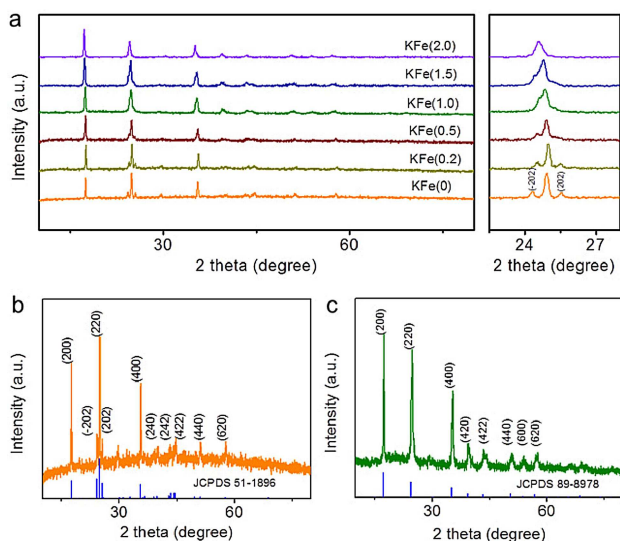

Figure 1. XRD patterns of a) all six samples, b) KFe(0), and c) KFe(1.0).

(space group P2$_1$/c) with a unit cell parameters of $a = 10.108$ Å, $b = 10.104$ Å, $c = 10.114$ Å, and $\beta = 92.938°$ (Figure 1b).[14] With the increase of hydrochloric acid concentration, the gradual disappearance of (−202) and (202) peaks indicates the structural changes from KFe(0) to KFe(2.0). The crystal structures of KFe(1.0), KFe(1.5) and KFe(2.0) can be confirmed as cubic phase (space group Fm-3m) instead of monoclinic phase (Figure 1c).[15] In addition, the half-peak width becomes broader with the increase of hydrochloric acid, suggesting a phenomenon of size decrease from KFe(0) to KFe(2.0) particles.[16]

In spite of their different crystal structures, KFe(0), KFe(0.2), KFe(0.5), and KFe(1.0) all display a similar cubic morphology. The average sizes of KFe(0) (Figure 2a and Figure S1), KFe(0.2) (Figure 2b), KFe(0.5) (Figure 2c), and KFe(1.0) (Figure 2d) are separately 1000, 300, 150, and 50 nm. And for KFe(1.5) (Figure 2e) and KFe(2.0) (Figure 2f), the average particle size continues to decrease (about 30 nm for KFe(1.5) and 20 nm for
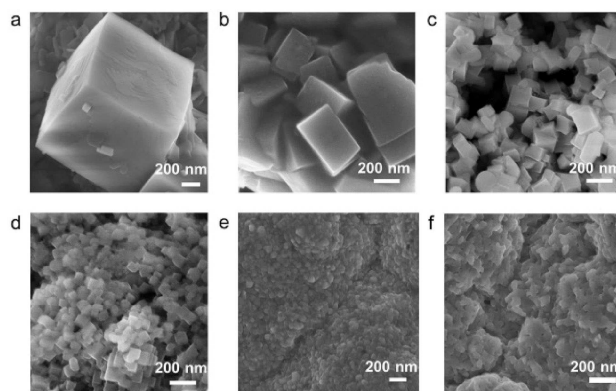

Figure 2. SEM images of a) KFe(0), b) KFe(0.2), c) KFe(0.5), d) KFe(1.0), e) KFe (1.5), and f) KFe(2.0).

KFe(2.0)), but the particle morphologies become irregular with obvious agglomeration can be observed. The results of XRD patterns and SEM images suggest that the size regulation can be achieved through changing the concentration of hydrochloric acid. This is mainly because [Fe(CN)$_6$]$^{4-}$ is slowly decomposed to Fe^{2+} in an acidic environment [Eq. (1)] and then Fe^{2+} reacts with the undecomposed [Fe(CN)$_6$]$^{4-}$ to form the Prussian white particles [Eq. (2)].[17]

$$Fe(CN)_6^{4-} \xrightarrow{H^+} Fe^{2+} + 6CN^- \tag{1}$$

$$Fe^{2+} + Fe(CN)_6^{4-} \rightarrow FeFe(CN)_6^{2-} \tag{2}$$
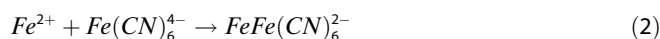
With the increase of hydrochloric acid concentration, more Fe^{2+} will be released at once, which can obtain numerous nucleation instantaneously. While the total amount of Fe species is limited, nanocrystallites form in the 1 mol L^{-1} hydrochloric acid environment.[18] When the concentration of hydrochloric acid is further increased, the excess release of Fe^{2+} enables this reaction process to be similar to a coprecipitation reaction. The fast reaction process leads to the irregular sample morphology, small particle size, easy agglomeration, low crystallinity and more defects.[7b,9b,17] The microstructures and crystal facets of all the samples were characterized by TEM and HRTEM images. Figure 3a–d clearly demonstrate that the particle sizes of KFe(0), KFe(0.2), KFe(0.5), and KFe(1.0) are about 1200, 300, 150, and 50 nm, respectively, which are consistent with the results derived from Figure 2a–d. KFe(1.5) (Figure 3e) and KFe(2.0) (Figure 3f) exhibit obvious agglomeration with irregular smaller particle size. The lattice-fringe distances simulated from Figure 3g-l are 0.357, 0.359, 0.504, 0.511, 0.359, and 0.362 nm, which can be separately assigned to the (220), (220), (200), (200), (220), and (220) crystal facets. It is noteworthy that the lattice fringes become more and more blurred from KFe(0) to KFe(2.0), which confirms that the crystallinity is gradually decreasing.

Considering that the K content controls the capacity delivery, the influence of acidity of hydrothermal environments on the formulas of all the samples, which were determined by the elemental analyzer for C, N, and H elements and inductively
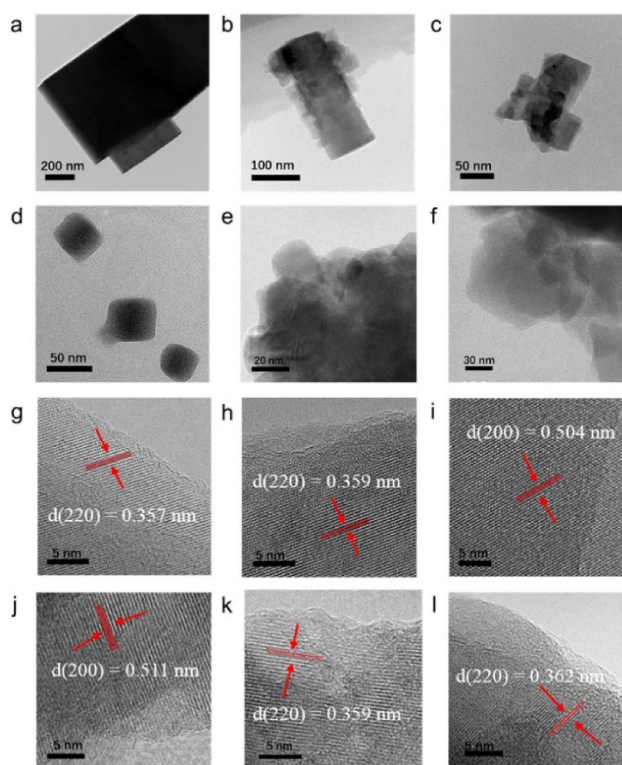
Figure 3. TEM images of a) KFe(0), b) KFe(0.2), c) KFe(0.5), d) KFe(1.0), e) KFe(1.5), and f) KFe(2.0). High-resolution TEM (HRTEM) images of g) KFe(0), h) KFe(0.2), i) KFe(0.5), j) KFe(1.0), k) KFe(1.5), and l) KFe(2.0).

coupled plasma atomic emission spectroscopy (ICP-AES) for Fe and K elements, is studied and the result is exhibited in Table S1. Based on the element analyses of K, Fe, C, N, and H, the six K-PW samples synthesized by using different concentrations of hydrochloric acid aqueous solutions are described by the formulas $K_{1.23}Fe[Fe(CN)_6]_{0.79} \cdot 0.08 H_2O$ (KFe(0)), $K_{1.35}Fe[Fe(CN)_6]_{0.80} \cdot 0.77 H_2O$ (KFe(0.2)), $K_{1.47}Fe[Fe(CN)_6]_{0.83} \cdot 1.07 H_2O$ (KFe(0.5)), $K_{1.93}Fe[Fe(CN)_6]_{0.97} \cdot 1.82 H_2O$ (KFe(1.0)), $K_{1.44}Fe[Fe$

$(CN)_6]_{0.88} \cdot 0.95 H_2O$ (KFe(1.5)), and $K_{1.25}Fe[Fe(CN)_6]_{0.83} \cdot 1.19 H_2O$ (KFe(2.0)), respectively. Therefore, the 1 mol L^{-1} hydrochloric acid aqueous solution induces the highest K content of 1.93 per formula with least $Fe(CN)_6$ vacancies, which is very close to the ideal component. In general, the K content is determined by the number of $Fe(CN)_6$ vacancies in the sample. The lower the $Fe(CN)_6$ vacancy, the higher the K content in the sample. However, for KFe(1.5) and KFe(2.0), the sample reacts rapidly during the preparation process, and Fe^{2+} may occupy the position of K, resulting in a low K content. Meanwhile, the ascorbic acid and N_2 conditions can prevent $Fe^{2+}/[Fe^{II}(CN)_6]^{4-}$ from being oxidized to $Fe^{3+}/[Fe^{III}(CN)_6]^{3-}$, which can also improve the K content.[19]

The surface chemical states of six samples are characterized by using X-ray photoelectron spectra (XPS). The Fe $2p_{3/2}$ deconvolution results of KFe(0), KFe(0.2), and KFe(0.5) displayed in Figure 4a–c all demonstrate a broad peak ranging from 705 to 712 eV, which can be fitted into two peaks of Fe^{2+} (708.5 eV) and Fe^{3+} (710.1 eV). And yet, as shown in Figure 4d-f, the Fe $2p_{3/2}$ deconvolution results of KFe(1.0), KFe(1.5) and KFe(2.0) only indicate the existence of Fe^{2+} species. Further calculation about area ratios between Fe^{3+} and Fe^{2+} peaks are simulated to be 0.263, 0.211, 0.102, 0, 0, and 0 respectively.

The electrochemical behaviors of different K-PW are assessed by CV and galvanostatic measurements in a three-electrode cell. As shown in Figure 5a, the CV curves of all electrodes show two pairs of oxidation-reduction peaks located at 0.1–0.4 V (vs. SCE) and 0.8–1.0 V (vs. SCE) tested at a scan rate of 1 mV s^{-1} in a 1.0 mol L^{-1} KNO_3 aqueous electrolyte. The two-electron redox reaction processes should be ascribed to the high-spin-state nitrogen-coordinated couple (Fe^{III}/Fe^{II}-N) and low-spin-state carbon-coordinated couple (Fe^{III}/Fe^{II}-C), respectively.[20] Figure 5b presents the 1st constant current charge/discharge curves of all electrodes at a current density of 75 mA g^{-1} (0.5 C, 1 C corresponds to 150 mA g^{-1}). All the curves in Figure 5b display two separated potential plateaus, which are in accordance with the two-electron redox reactions in CV curves. The KFe(1.0) electrode delivers a high reversible
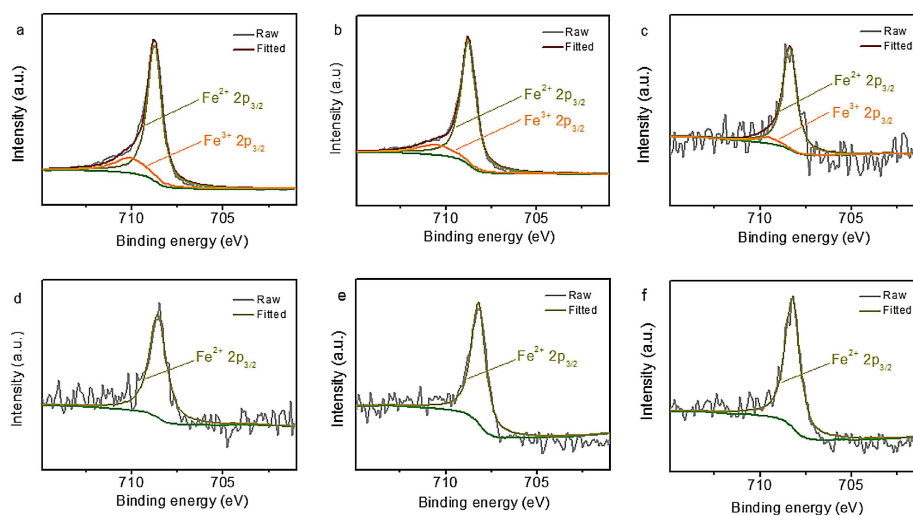

Figure 4. Fe $2p_{3/2}$ XPS spectra of a) KFe(0), b) KFe(0.2), c) KFe(0.5), d) KFe(1.0), e) KFe(1.5), and f) KFe(2.0).
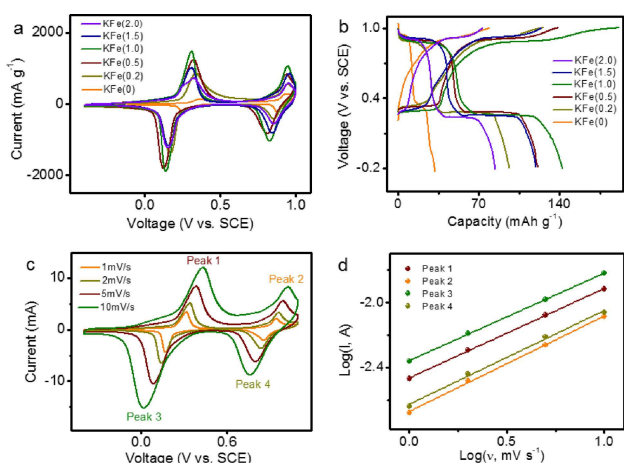
Figure 5. Electrochemical properties of all samples. a) CV curves of all the samples performed at a scan rate of 1 mV s^{-1} in a 1.0 mol L^{-1} KNO$_3$ aqueous electrolyte. b) Galvanostatic charge/discharge curves of all the samples (1st cycle) at a current density of 75 mA g^{-1}. c) CV curves of the KFe(1.0) at the different scan rates from 1 to 10 mV s^{-1}. d) Linear relation of log(I, peak current) and log(v, scan rate) based on the CV curves of KFe(1.0).

Figure 6. Battery performances of all samples. a) Specific capacities tested at different current densities from 75 (0.5 C) to 9000 mA g^{-1} (60 C). b) Cycling performances tested at 1500 mA g^{-1} (10 C).

discharge capacity of 142 mAh g^{-1}, which should be attributed to its highest K content and least Fe(CN)$_6$ vacancies. While much lower discharge capacities of 33, 96, 122, 119, and 85 mAh g^{-1} are separately delivered for the KFe(0), KFe(0.2), KFe(0.5), KFe(1.5), and KFe(2.0) electrodes. The charge specific capacity is higher than the discharge specific capacity because oxygen evolution reaction occurs during charging process. As exhibited in Figure 5c, the CV curves of KFe(1.0) electrode show two pairs of sharp oxidation-reduction peaks at different scan rates within 1 and 10 mV s^{-1}. The increase of scan rate leads to the improved peak currents and overpotentials. As displayed in Figure 5d, two oxidation peaks and two reduction peaks all exhibit a plot of log(I) versus log(v) based on the CV curves. The simulated values of slope for the two cathodic peaks are 0.55 and 0.58, and two anodic peaks are 0.53 and 0.57, respectively, suggesting the domination of ion-diffusion behavior in the kinetics of KFe(1.0) electrode in a 1 mol L^{-1} KNO$_3$ electrolyte. For the KFe(0), KFe(0.2), KFe(0.5), KFe(1.5), and KFe(2.0) electrodes (Figure S2-S6 and Table S2), they also reveal a ion-diffusion-controlled insertion mechanism in a 1 mol L^{-1} KNO$_3$ electrolyte.

Figure 6a exhibits the specific capacities of all electrodes tested at different current densities. With the increase of current densities from 75 (0.5 C) to 9000 mA g^{-1} (60 C), the KFe(1.0) electrode delivers the highest specific capacities from 142 to 40 mAh g^{-1} at all current densities (from 0.5 to 60 C). The KFe(1.0), KFe(1.5) and KFe(2.0) possess smaller particle size among the six samples, which indicates shorter K$^+$-diffusion length and smaller volume expansion during the ion-diffusion-controlled extraction/insertion processes.[21] And KFe(1.0) has higher crystallinity than that of KFe(1.5) and KFe(2.0). Combining these two factors, excellent rate capability in KFe(1.0) is realized. Figure 6b shows the cycling performances of six samples performed at 1500 mA g^{-1} (10 C). All the electrodes display remarkable cycling stability, and among which the KFe(1.0) electrode shows the highest capacity delivery. The capacity delivery of KFe(1.0)
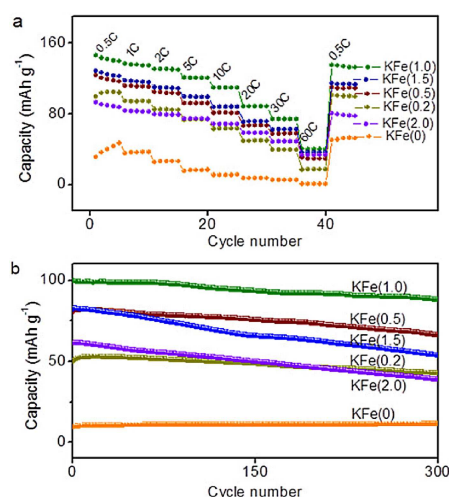
electrode only decreases from 100.1 to 88.2 mAh g^{-1} after 300 cycles, i.e., a high capacity retention of 88%. The superior structural stability insured by high crystallinity suppresses the dissolution of active material in aqueous electrolytes, and nano-sized engineering improves the long-term cycling stability. In contrast, although the particle sizes of KFe(1.5) and KFe(2.0) are smaller, poor crystallinity makes them more soluble in aqueous solution, leading to inferior cycling performances. In addition, the XRD pattern and SEM image of KFe(1.0) electrode cycled after 300 cycles are consistent with the initial results (Figure S7), which further affirm the structural stability of KFe(1.0).

A further ex-situ XRD test was carried out to assess the stability of KFe(1.0) electrode. Figure 7 shows the ex-situ XRD
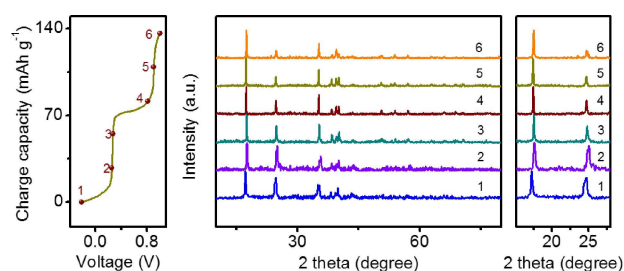

Figure 7. Ex situ XRD patterns of KFe(1.0) electrode collected at various charged states.

patterns of KFe(1.0) electrode collected at different charged states. During the charging process, six nodes (labelled as 1–6) with specific capacities of 0, 20%, 40%, 60%, 80%, and 100% at a current density of 150 mA g^{-1} (1 C) were selected, respectively. The peaks positions of all XRD patterns show almost no change, implying that no significant crystal transformation occurs and only a slight change of lattice parameter happens during the K$^+$ extraction process, which confirms the stability of KFe(1.0) sample. A comparison between the KFe(1.0)
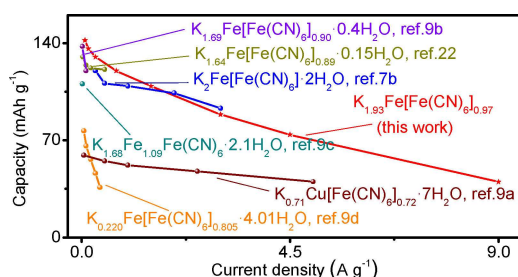
Figure 8. Rate performance of the KFe(1.0) electrode compared to that of some previously reported K-PW cathodes.[7b,9,22]

electrode and other reported K-PW cathodes is displayed in Figure 8. It can be seen that the reversible capacity and rate capability of KFe(1.0) electrode is greater than those of other reported K-PW materials.

3. Conclusions

In summary, K-PW samples with different particle sizes and crystallinity have been synthesized through hydrothermal method by controlling the acidic environments. The high-crystallinity KFe(1.0) ($K_{1.93}Fe[Fe(CN)_6]_{0.97} \cdot 1.82H_2O$) species comprised of 50 nm crystallites delivers the highest reversible capacity and rate capability. Discharge capacities of 142 mAh g^{-1} at 75 mA g^{-1}, 130 mAh g^{-1} at 300 mA g^{-1}, and even 40 mAh g^{-1} at 9000 mA g^{-1} are achieved, and high capacity retention of 88% is realized after 300 cycles at 1500 mA g^{-1} in KNO$_3$ aqueous solution for the KFe(1.0) electrode. The high potassium content of KFe(1.0) ensures high capacity delivery, and the high crystallinity and nano-size engineering favor the high rate performance and long-term cycling stability. The low-cost and easy-synthesis Prussian white analogues provide a new insight into the design of electrode materials for aqueous KIBs and other battery systems.

Experimental Section

Synthesis of the Prussian White Analogues

All chemicals were obtained from Sinopharm Chemical Reagent Co. Ltd (China) and were used without further treatment. In a typical procedure, 4 mmol of K$_4$Fe(CN)$_6$ (AR) and 1 g ascorbic acid (AR) were dissolved in 120 mL of hydrochloric acid aqueous solution of 0, 0.2, 0.5, 1.0, 1.5, and 2.0 mol L^{-1}, respectively, under stirring. In order to eliminate the oxygen dissolved in water, the obtained solutions were bubbled with N$_2$ for 30 minutes. Then the above solutions were mixed at 70 °C for 4 h under N$_2$ protection. After cooled to room temperature, the samples were collected by centrifugation, washed by water and ethanol for three times, respectively. Finally, the samples were dried at 110 °C under vacuum for 12 h.

Materials Characterization

The crystal structures of the samples were characterized by X-ray diffraction (XRD, Bruker D8 Advance diffractometer) with Cu K_α radiation ($\lambda = 1.5405$ Å). The morphology and size of obtained samples were examined by scanning electronic microscopy (SEM, ZEISS Supra 55) and transmission electron microscopy (TEM, FEI Tecnai G2 F20 s-Twin). The chemical compositions was examined by inductively coupled plasma atomic emission spectroscopy (ICP-AES, Horiba Jobinyvon JY2000-2) for K and Fe elements and by the element analysis (Vario EL cube) for C, N and H elements.

Preparation of the Electrodes and Electrochemical Tests

All the electrochemical properties of the K-PW samples were performed at room temperature using a half-cell configuration. The K-PW samples were mixed with conductive material (Ketjen black), and binder (polytetrafluoroethylene, PTFE) at a weight ratio of 7:2:1 with the diluent of isopropyl alcohol. The mixture was pressed into film to cut into disks and then dried at 110 °C for 12 h under vacuum. After dying, these disks were pressed onto Ti mesh to be used as the working electrode. The average mass loading of the electrodes is 1.45 mg cm^{-2}. The counter electrode was prepared in the same way as the above working electrode with the mixture of activated carbon (AC), acetylene black and PTFE at a weight ratio of 8:1:1. The cyclic voltammetric (CV) tests and galvanostatic measurements of the K-PW electrodes were carried out in KNO$_3$ (1 mol L^{-1}) aqueous solution by using a three-electrode system. The system is consist of the above working electrode, counter electrode, and saturated calomel electrode (SCE). The CV measurements were conducted at various scan rates on a CHI660D electrochemical workstation (Chenhua Instrument Company, Shanghai, China). The electrochemical tests were measured on a NEWARE battery test system. The relationship between peak current and scan rate can be described as the following equation [Eq. (3)]:

$$I = a\nu^b \tag{3}$$

where I is peak current (A) and ν is scan rate (mV s^{-1}).[7b] Generally, if the value of b is 0.5, it would be a diffusion-controlled insertion.[7b,15]

Conflict of Interest

The authors declare no conflict of interest.

[1] a) X. Su, Q. Wu, J. Li, X. Xiao, A. Lott, W. Lu, B. W. Sheldon, J. Wu, *Adv. Energy Mater.* **2014**, *4*, 1300882; b) X. Wang, K. Du, C. Wang, L. Ma, B. Zhao, J. Yang, M. Li, X. X. Zhang, M. Xue, J. Chen, *ACS Appl. Mater. Inter.*

2017, *9*, 38606–38611; c) E. A. Olivetti, G. Ceder, G. G. Gaustad, X. Fu, *Joule* **2017**, *1*, 229–243.

[2] a) D. P. Dubal, O. Ayyad, V. Ruiz, P. Gomez-Romero, *Chem. Soc. Rev.* **2015**, *44*, 1777–1790; b) Z. Yu, L. Tetard, L. Zhai, J. Thomas, *Energy Environ. Sci.* **2015**, *8*, 702–730; c) X. Ma, M. Xue, F. Li, J. Chen, D. Chen, X. Wang, F. Pan, G. F. Chen, *Nanoscale* **2015**, *7*, 8715–8719; d) M. Xue, D. Chen, X. Wang, J. Chen, G. F. Chen, *J. Mater. Chem. A* **2015**, *3*, 7715–7718.

[3] L. Grande, E. Paillard, J. Hassoun, J. B. Park, Y. J. Lee, Y. K. Sun, S. Passerini, B. Scrosati, *Adv. Mater.* **2015**, *27*, 784–800.

[4] A. Manthiram, Y. Fu, S. H. Chung, C. Zu, Y. S. Su, *Chem. Rev.* **2014**, *114*, 11751–11787.

[5] a) D. Aurbach, Y. Gofer, Z. Lu, A. Schechter, O. Chusid, H. Gizbar, Y. Cohen, V. Ashkenazi, M. Moshkovich, R. Turgeman, E. Levi, *J. Power Sources* **2001**, *97–98*, 28–32; b) C. Xu, B. Li, H. Du, F. Kang, *Angew. Chem. Int. Ed. Engl.* **2012**, *51*, 933–935; c) A. Ponrouch, C. Frontera, F. Barde, M. R. Palacin, *Nat. Mater.* **2016**, *15*, 169–172; d) M. C. Lin, M. Gong, B. Lu, Y. Wu, D. Y. Wang, M. Guan, M. Angell, C. Chen, J. Yang, B. J. Hwang, H. Dai, *Nature* **2015**, *520*, 325–328.

[6] a) X. Wang, D. Chen, Z. Yang, X. Zhang, C. Wang, J. Chen, X. Zhang, M. Xue, *Adv. Mater.* **2016**, *28*, 8645–8650; b) X. Wang, Z. Yang, C. Wang, D. Chen, R. Li, X. Zhang, J. Chen, M. Xue, *J. Power Sources* **2017**, *369*, 138–145; c) X. Wang, Z. Yang, C. Wang, L. Ma, C. Zhao, J. Chen, X. Zhang, M. Xue, *Nanoscale* **2018**, *10*, 800–806; d) C. D. Wessells, S. V. Peddada, R. A. Huggins, Y. Cui, *Nano Lett.* **2011**, *11*, 5421–5425; e) Z. Jian, Z. Xing, C. Bommier, Z. Li, X. Ji, *Adv. Energy Mater.* **2016**, *6*, 1501874.

[7] a) N. Alias, A. A. Mohamad, *J. Power Sources* **2015**, *274*, 237–251; b) D. Su, A. McDonagh, S. Z. Qiao, G. Wang, *Adv Mater* **2017**, *29*, 1604007; c) R. Trocoli, F. La Mantia, *ChemSusChem* **2015**, *8*, 481–485; d) W. Li, J. R. Dahn, D. S. Wainwright, *Science* **1994**, *264*, 1115–1118; e) Q. Qu, L. Li, S. Tian, W. Guo, Y. Wu, R. Holze, *J. Power Sources* **2010**, *195*, 2789–2794; f) Q. T. Qu, Y. Shi, S. Tian, Y. H. Chen, Y. P. Wu, R. Holze, *J. Power Sources* **2009**, *194*, 1222–1225; g) W. Tang, L. L. Liu, S. Tian, L. Li, Y. B. Yue, Y. P. Wu, S. Y. Guan, K. Zhu, *Electrochem. Commun.* **2010**, *12*, 1524–1526; h) W. Tang, S. Tian, L. L. Liu, L. Li, H. P. Zhang, Y. B. Yue, Y. Bai, Y. P. Wu, K. Zhu, *Electrochem. Commun.* **2011**, *13*, 205–208.

[8] Z. Shadike, D.-R. Shi, T.-W. Tian-Wang, M.-H. Cao, S.-F. Yang, J. Chen, Z.-W. Fu, *J. Mater. Chem. A* **2017**, *5*, 6393–6398.

[9] a) C. D. Wessells, R. A. Huggins, Y. Cui, *Nat. Commun.* **2011**, *2*, 550; b) G. He, L. F. Nazar, *ACS Energy Lett.* **2017**, *2*, 1122–1127; c) X. Wu, Z. Jian, Z. Li, X. Ji, *Electrochem. Commun.* **2017**, *77*, 54–57; d) C. Zhang, Y. Xu, M. Zhou, L. Liang, H. Dong, M. Wu, Y. Yang, Y. Lei, *Adv. Funct. Mater.* **2017**, *27*, 1604307.

[10] C. D. Wessells, S. V. Peddada, M. T. McDowell, R. A. Huggins, Y. Cui, *J. Electrochem. Soc.* **2011**, *159*, A98-A103.

[11] a) B. Wenger, P. K. Nayak, X. Wen, S. V. Kesava, N. K. Noel, H. J. Snaith, *Nat. Commun.* **2017**, *8*, 590; b) H. Wei, D. DeSantis, W. Wei, Y. Deng, D. Guo, T. J. Savenije, L. Cao, J. Huang, *Nat. Mater.* **2017**, *16*, 826–833.

[12] M. Xue, Y. Wang, X. Wang, X. Huang, J. Ji, *Adv. Mater.* **2015**, *27*, 5923–5929.

[13] H. Liang, X. Ma, Z. Yang, P. Wang, X. Zhang, Z. Ren, M. Xue, G. Chen, *Carbon* **2016**, *99*, 585–590.

[14] M. Hu, J. S. Jiang, *Mater. Res. Bull.* **2011**, *46*, 702–707.

[15] L. Zhou, M. Zhang, Y. Wang, Y. Zhu, L. Fu, X. Liu, Y. Wu, W. Huang, *Electrochim. Acta* **2017**, *232*, 106–113.

[16] L. Z., M. R., O. M., I. N., E. Y., T. K., S. T., *J. Am. Chem. Soc.* **2006**, *128*, 4872–4880.

[17] Y. You, X.-L. Wu, Y.-X. Yin, Y.-G. Guo, *Energy Environ. Sci.* **2014**, *7*, 1643–1647.

[18] G. Cao, *Nanostructures and nanomaterials: synthesis, properties and applications*, World Scientific, **2004**, pp. 41–78.

[19] Y. You, X. Yu, Y. Yin, K.-W. Nam, Y.-G. Guo, *Nano Res.* **2014**, *8*, 117–128.

[20] a) Y. Lu, L. Wang, J. Cheng, J. B. Goodenough, *Chem. Commun. (Camb.)* **2012**, *48*, 6544–6546; b) L. Wang, J. Song, R. Qiao, L. A. Wray, M. A. Hossain, Y. D. Chuang, W. Yang, Y. Lu, D. Evans, J. J. Lee, S. Vail, X. Zhao, M. Nishijima, S. Kakimoto, J. B. Goodenough, *J. Am. Chem. Soc.* **2015**, *137*, 2548–2554.

[21] Y. Jiang, Y. Yu, B. Wang, Y. Li, W. Sun, Y. Lu, M. Yan, B. Song, S. Dou, *Adv. Funct. Mater.* **2016**, *26*, 5315–5321.

[22] X. Bie, K. Kubota, T. Hosaka, K. Chihara, S. Komaba, *J. Mater. Chem. A* **2017**, *5*, 4325–4330.